IEEE Access
Multidisciplinary ⋮ Rapid Review ⋮ Open Access Journal

Received 12 April 2026, accepted 6 May 2026, date of publication 12 May 2026, date of current version 15 May 2026.
Digital Object Identifier 10.1109/ACCESS.2026.3691976

RESEARCH ARTICLE

A Rotation-Controlled Anisotropic Hourglass Metasurface for Multiband Reflective Linear-to-Circular and Cross-Polarization Conversion

MUHAMMAD NASIR [1], SLAWOMIR KOZIEL [1,2], (Fellow, IEEE), AND ANNA PIETRENKO-DABROWSKA [2], (Senior Member, IEEE)
[1]Engineering Optimization and Modeling Center, Reykjavík University, 102 Reykjavík, Iceland
[2]Faculty of Electronics, Telecommunications and Informatics, Gdańsk University of Technology, 80-233 Gdańsk, Poland

Corresponding author: Slawomir Koziel (koziel@ru.is)

This work was supported in part by Icelandic Research Fund under Grant 2410297, and in part by the National Science Center of Poland under Grant 2022/47/B/ST7/00072.

ABSTRACT This paper presents and experimentally validates a multifunctional anisotropic metasurface (MS) that exhibits linear-to-linear (LTL) reflective cross-polarization (RCP) and circular polarization conversion (CPC) responses across multiple frequency ranges. The proposed MS integrates a single-layer design consisting of 45° oriented truncated circular ring and an hourglass-like structure, providing four LTL-RCP conversion bands (2.41 – 2.48, 3.16 – 3.46, 5.80 – 6.59, and 11.64 – 13.75) GHz with polarization conversion ratio (PCR) exceeding 95%, and seven CPC bands (2.33 – 2.38, 2.55 – 2.99, 3.69 – 5.37, 7.13 – 10.92, 13.95 – 14.25, 14.93 – 15.17, and 15.31 – 15.56) GHz with the axial ratio (AR) less than 3 dB, covering the S-, C-, X-, and Ku-bands. By only adjusting the angle of the hourglass structure at 15° within the same structure, LTL-RCP with PCR greater than 95% is realized in the frequency bands from 13.71 to 14.64 GHz, along with $\leq$ 3 dB of AR is achieved at four additional CPC bands at (2.20 – 2.36, 2.95 – 8.41, 10.84 – 12.30, and 14.84 – 15.06) GHz. The polarization conversion mechanisms are explained through detailed surface-current distributions analysis and full-wave electromagnetic (EM) simulations. Furthermore, the proposed concept is validated through the measurements of the fabricated prototype consisting of 8 $\times$ 13-unit cells. The measurement results are in excellent agreement with the simulation predictions. The proposed MS design demonstrates a simple yet effective solution for achieving tunable multi-band polarization manipulation without structural modification, making it suitable for advanced EM communication applications.

INDEX TERMS Reflective circular polarization, reflective cross polarization conversion, multiband, multifunctional, polarization conversion ratio, axial ratio, communication application.

I. INTRODUCTION

The MS structures, consisting of periodically arranged sub-wavelength resonators, provide compactness, low cost, and efficient solutions for manipulating EM waves [1], [2]. MSs utilize the EM coupling and structural isotropy/anisotropy to effectively control the magnitude, phase, and polarization [3], [4], [5], [6]. As a result, it can be used for diverse applications, such as radar stealth technology, wireless communication, and antenna design [7], [8], [9]. Recent studies reveal that the MS structures have significant potential to realize EM wave polarization conversion. For example, Yang et al. [10] reported a split-square-ring-based reconfigurable MS that combines cross- and circular-polarization (circular-pol.)

The associate editor coordinating the review of this manuscript and approving it for publication was Davide Ramaccia.

conversions in reflection along with other EM properties by changing the state of the integrated PIN diode. Another reconfigurable MS in [11] combines orthogonal strip gratings in a multilayer structure, retaining LTL cross-polarization (cross-pol.) conversion in reflection and transmission. Furthermore, butterfly-shaped patches integrated with PIN diodes are studied in [12], yielding multiple LTL-RCP and CPC bands depending on the diode switching state. Reference [13] proposes symmetrical L-shaped patch structures that utilize PIN diodes to toggle between LTL-RCP conversion and CPC characteristics. In general, the switching state of the integrated diodes allows the MS to tailor EM response, enabling controlled switching or achieving RCP and CPC functionalities [14]. The high flexibility in achieving multiband and multifunctionality with PIN diodes results in increased biasing complexity, integration challenges, and fabrication costs when integrated into MS array structures.

Alternatively, this issue can be addressed by adopting the anisotropic configuration of the MS. Accordingly, a recent study in [15] proposed an ellipse-shaped anisotropic MS, which achieved two RCP conversion and CPC bands. Another single-layer H-shaped cross-pol. converter MS realized multiband cross-pol. conversion, including Penta RCP and Octa CPC bands [16]. In [17], two RCP conversion bands along with a CPC are realized by loading a circular disk inside the split ring resonator (SRR) structure. Similarly, another SRR-loaded cross-dipole pattern design is proposed in [18], which combines multiband reflective polarization transformation combining CPC and RCP characteristics. Moreover, a single-layer C-shaped anisotropic unit-cell structure in [19] is studied for reflective polarization conversion across C-, X-, and K-bands. There are plenty of other anisotropic MS structures that have been studied, proposed, and experimentally verified, to obtain LTL-RCP conversion and CPC characteristics at multiple frequency bands, such as, a combination of ring and square elements [20], four semicircles with different radii on the four sides of the unit cell [21], a slotted rectangular I-shaped meta-atom [22], two periodically arranged SRR with a slotted stripe [23], coupled SRRs unit [24], circular SRR with an inside a cross shape structure [25], a rectangular slot based circular ring with an additional partial circle structure [26], and one diagonal stub along with an annular ring embedded with a strip [27]. Nonetheless, most reported designs focus either on increasing the operating bands by employing active components or multilayer structures. Limited effort has been made to exploit structural mechanisms to realize orientation-dependent polarization states.

This work proposes a single-layer hourglass-inspired anisotropic meta-atom combined with an outer square ring, which supports multi-resonant coupling, enabling linear polarization (LP) to LTL-RCP conversion and CPC (LHCP/RHCP) in eleven bands by keeping the rotation of the hourglass at 45°. By adjusting the rotation angle of an hourglass to 15°, the proposed MS achieves four CPC (LHCP/RHCP) bands along with an LTL-RCP conversion band. Compared to previous research, the proposed work retains advantages such as wideband performance, high flexibility, multiband operation, and multifunctional characteristics.

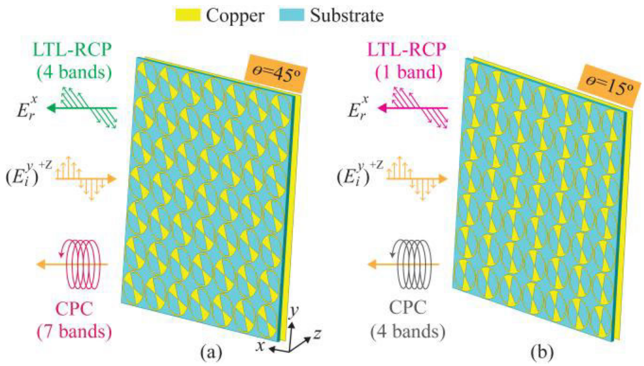

FIGURE 1. Perspective view of the proposed MS array illustrating the conceptual understandings of polarization conversion functionalities under $+Z$-directed incident waves, for (a) $\theta = 45°$ and (b) $\theta = 15°$ rotated hourglass.

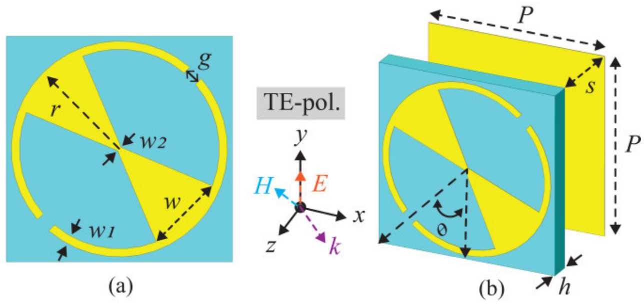

FIGURE 2. Proposed MS (a) front view, (b) perspective view. The optimized dimensions are [P = 14, r = 6.7, w = 6, w_1 = 0.5, w_2 = 0.3, g = 1, s = 3.5, h = 1.6] mm, and $\theta = 45°$.

II. DESIGN DESCRIPTION

Fig.s 1(a) and 1(b) illustrate the conceptual background of the achieved multiple polarization conversion bands of the proposed MS. It is a single-layer anisotropic structure, comprising an hourglass meta-atom combined with a slotted resonant ring, printed on the FR4 substrate ($\varepsilon_r = 4.3$ and $\tan\delta = 0.025$) having a thickness of 1.6 mm and backed by a ground plane. A comprehensive depiction of the precise dimensions and geometrical configuration of the proposed MS is provided in Figures 2(a) and 2(b), respectively. By changing the rotation angle θ of the hourglass w.r.t the y-axis, multiple polarization conversion functions can be realized.

This study evaluates the efficiency of LTL cross-pol. conversion and CPC in reflection, using the PCR and AR conditions, with the acceptance criteria of > 90% for LTL-RCP and ≤ 3 dB of AR for CPC bands. Thereafter, we define [28];

$$\mathrm{PCR} = (R_{xy}^2/(R_{xy}^2 + R_{yy}^2) \quad (1)$$

$$\mathrm{AR} = \left(\frac{|R_{yy}|^2 + |R_{xy}|^2 + \sqrt{q}}{|R_{yy}|^2 + |R_{xy}|^2 - \sqrt{q}} \right)^{0.5} \quad (2)$$

where,

$$q = \left[|R_{yy}|^4 + |R_{xy}|^4 + 2\,|R_{yy}|^2\,|R_{yy}|^2 \cos\left(2\Delta\varphi_{xy}\right) \right] \quad (3)$$

To verify these conditions, full-wave EM simulations are performed using CST Microwave Studio with y-polarized incident waves and are assumed to impinge normally from the $+Z$-direction. In the following, we denote reflective co- and cross-components as: $R_{yy} = |E_r^y/E_i^y|$, $R_{xy} = |E_r^x/E_i^y|$. Therein, E_r^y and E_r^x (E_i^y) are the reflected (incident) E-field components in the y-direction.

III. DESIGN EVOLUTION METHODOLOGY

Based on the principle of symmetrically decomposed u- and v-polarized wave components, the efficiency of cross-pol. conversion reaches its maximum value when the u- and v-polarized components are aligned 45° w.r.t the direction of the polarization converter surface [28]. Under this condition, one component undergoes reflection with a 0° phase shift, enabling a high-impedance surface (HIS) behavior. While the second component reflects with 180° phase shift, which acts as a perfect electric conductor (PEC) [28], [29]. Consequently, cross-pol. rotation (y to x) occurs w.r.t the incident wave (E_i), thereby leading to the LTL-RCP transformation. On the other hand, when the magnitudes of reflected decomposed components are equal, and their phase difference is 90 degrees [$\Delta\varphi r_{uv} = arg\,(\varphi_{ru}) - arg\,(\varphi_{rv}) \approx 90°$], the E_i is converted into the circularly polarized reflected wave [28].

It is important to mention that, due to the symmetry existence in the proposed MS along the u- and v-axis, the polarization conversion (PC) in reflection responses remains identical under both x- and y-polarization excitations. Therefore, for simplicity, only the y-polarized (TE-pol.) incident response is considered for further analysis.

To validate the above discussion, a circular ring with diagonally truncated cuts, along with a 45° rotated hourglass is introduced, where each resonator collectively contributes to generating the multiple PC bands. Retaining multiple PC bands in a single passive MS design is challenging because it typically requires a multi-resonant or multilayer structure [12], [21]. Therefore, an optimized taper design (forming a complete hourglass when copied in a mirror) is used to maintain a high-efficiency response of the PC. Moreover, the polarization transformation across multiple bands of the proposed surface layer is verified stepwise using simulated results, as shown in Figures 3(a) - 3(f).

Initially, at Stage-1, a narrow circular ring is considered based on the following equation; $f_{res} = \frac{c_0}{2\pi r\sqrt{\varepsilon_{eff}}}$ [30], where f_{res}, C_0, r, and ε_{eff} are the resonance, speed of light, radius of the ring, and effective permittivity, respectively. In Figure 3(a), the simulated response of the circular ring reveals ≤ -10 dB co-polarized (co-pol.) reflection R_{yy} and > -1 dB cross-pol. reflection R_{xy} at 3.03 – 3.28 GHz, and 5.82 – 7.07 GHz. While the R_{yy} and R_{xy} components achieved -3 dB (i.e., $|R_{xx}|^2 = |0.707|^2 = 0.5$ and $|R_{yx}|^2 = |0.707|^2 = 0.5$) values at three frequency bands of 2.85 – 2.89 GHz, 3.65 – 4.86 GHz, and 8.40 – 9.72 GHz, suggesting that the Stage-1 acts as a dual-band LTL-RCP and tri-band circular pol. converter, as also confirmed by the PCR > 90% and AR < 3 dB, depicted in Figure 3(b).

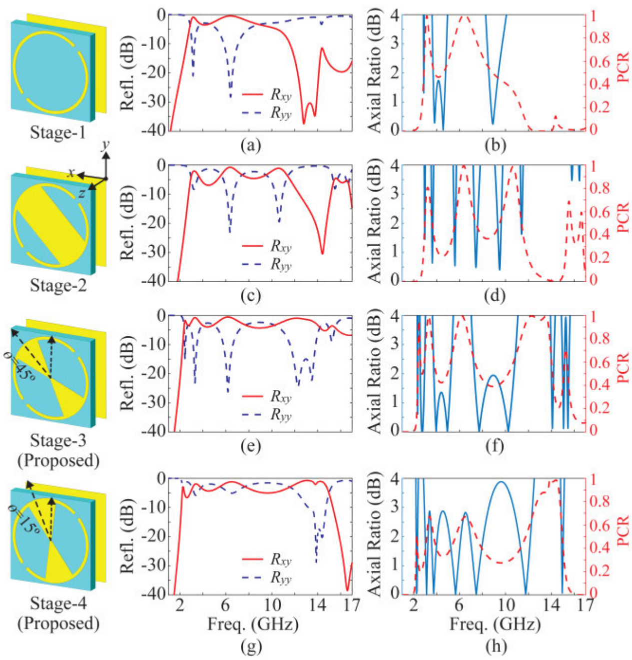

FIGURE 3. Stepwise simulated EM response of the truncated circular ring, diagonal strip with truncated circular ring, and proposed hourglass surface: (a), (c), (e), and (g) co- and cross-pol. reflection results (b), (d), (f), and (h) correspond to AR and PCR responses.

In Stage-2, a diagonal strip is inserted with the truncated circular ring, which results in a dual LTL-RCP conversion at 6.10 – 6.64 GHz, 10.35 – 10.90 GHz, and six CPC bands at 2.90 – 3.05 GHz, 3.55 – 3.70 GHz, 5.48 – 5.69 GHz, 7.23 – 7.68 GHz, 9.20 – 9.68 GHz, and 11.31 – 11.48 GHz, as evidenced in Figures 3(c) and 3(d), respectively.

Then in Stage-3, a tapered configuration (usually used to obtain multiband and wideband response [31], [32]) is adopted to improve the performance, which results in quad LTL-RCP conversion at 2.41 – 2.48 GHz, 3.16 – 3.46 GHz, 5.80 – 6.59 GHz, and 11.64 – 13.75 GHz, along with seven CPC bands at 2.33 – 2.38 GHz, 2.55 – 2.99 GHz, 3.69 – 5.37 GHz, 7.13 – 10.92 GHz, 13.95 – 14.25 GHz, 14.93 – 15.17 GHz, and 15.31 – 15.56 GHz, as shown in Figures 3(e) and 3(f). Notably in Figure 3(f), the adoption of taper configuration leads to obtaining wideband and multiband cross- and circular-pol. responses as compared to Figure 3(d), and this is exactly what we desired, because such a response can serve for a communication application where multiple bands remain of paramount importance.

Next, at Stage-4, the hourglass is rotated (θ) at 15° w.r.t y-axis, altering the phase and magnitude of the reflected

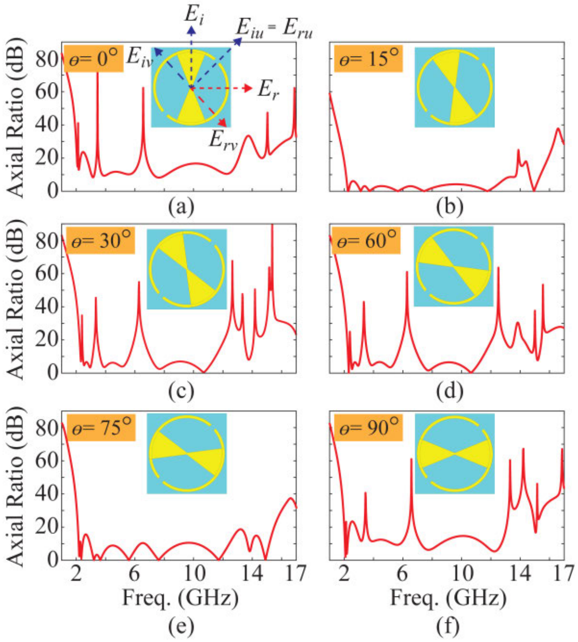

FIGURE 4. Axial ratio results for (a) 0°, (b) 15°, (c) 30°, (d) 60°, (e) 75°, and (f) 90° rotation angles.

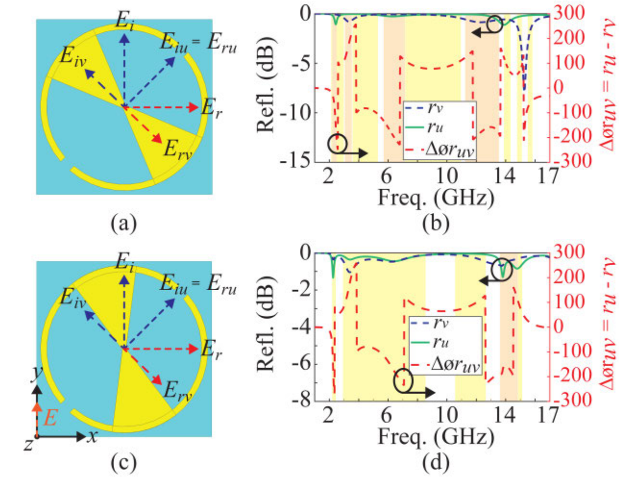

FIGURE 5. E_i decomposition on the (a) 45°, (c) 15° rotated hourglass MS, (b) and (d) corresponding reflection magnitudes of the *u*- and *v*-components and their phase difference ($\Delta\phi r_{uv}$).

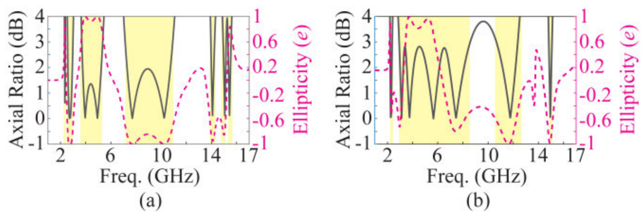

FIGURE 6. Ellipticity with axial ratio of (a) 45°, and (b) 15° rotated hourglass.

components, thereby retaining quad CPC bands at the frequency range of 2.20 – 2.36 GHz, 2.95 – 8.41 GHz, 10.84 – 12.30 GHz, and 14.84 – 15.06 GHz, along with an RCP band from 13.71 to 14.64 GHz, as verified in Figures 3(g) and 3(h). Conclusively, the proposed MS structure and presence of the dielectric slab (h) with an air layer (s) introduce additional reflections, resulting in a multiband response totaling sixteen bands, including five LTL-RCP conversion bands and eleven CPC bands, respectively.

IV. WORKING PRINCIPLE

To gain more insight into the physical mechanism behind LTL-RCP conversion and CPC of the proposed MS, we examine the incident wave (E_i) decomposition into two orthogonal u- and v-wave components. This involves only rotating the hourglass counterclockwise, as shown in Figure 4. As the hourglass rotates, the conditions required for CPC change accordingly. The results given in Figures 4(a) – 4(f) reveal that when the symmetry coincides with the decomposed u- and v-components axis, the AR appears < 3 dB, indicating successful CPC phenomena at multiple bands. Conversely, polarization conversion cannot be achieved when the symmetry axis is not aligned with the decomposed u- and v-axes. Conclusively, multiband CPC performance can be obtained when the symmetry axis of the hourglass MS coincides with the u- and v-axes, as evidenced at 15° and 75° in Figures 4(b) and (e), respectively. Further analysis of Figure 4 reveals that, upon counterclockwise rotation, the distance from the truncated cut of the circular ring and hourglass varies, which intuitively alters the relative phase and magnitude of the orthogonal field components, leading to different polarization states. This behavior is consistent with the results shown in Figure 4, where different rotation angles yield distinct axial-ratio characteristics. Therefore, the 15° orientation of the hourglass is selected to achieve the desired circular-pol. response.

To further understand the polarization conversion mechanism, we use the u- and v-coordinate system for LTL-RCP conversion (45° rotation) and CPC (15° rotation) of the hourglass models. When E_i impinges on the 45° rotated hourglass MS, it is decomposed into two orthogonal u- and v-wave components, as interpreted by the following equation:

$$E_i = \hat{u}\, E_{iu} e^{j\emptyset_{iu}} + \hat{v}\, E_{iv} e^{j\emptyset_{iv}} \quad (4)$$

where E_{iu} and E_{iv} represent the amplitudes of transmitted (u-) and reflected (v-) components with the corresponding phases $\emptyset_{iu}$ and $\emptyset_{iv}$, respectively. The full illustration of the E_i wave decomposition and its reflections are illustrated in Figures 5(a) and 5(c), respectively. The collective reflected components can be expressed as $E_r = \hat{u} r_u E_{ru} e^{j\emptyset_{ru}} + \hat{v} r_v E_{rv} e^{j\emptyset_{rv}}$. Here, $r_u e^{j\emptyset_{ru}}$ and $r_v e^{j\emptyset_{rv}}$ are the complex reflection coefficients along u- and v-axes. The E_i decomposition into u and v and their subsequent reflections from the MS leads to obtaining one component, 0° phase shift (*HIS*), and 180° phase shift to the second component (*PEC*). Consequently, orthogonal polarization (i.e., 90° rotation - LTL-RCP

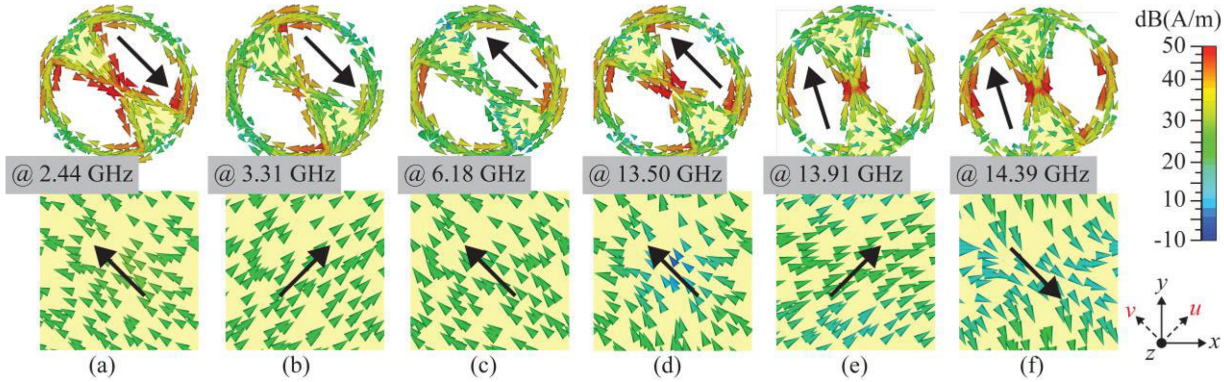

FIGURE 7. Surface current distribution on the top-layer (*first row*) and bottom-layer (*second row*), at the resonant frequencies: (a) 2.44 GHz, (b) 3.31 GHz, (c) 6.18 GHz, (d) 13.50 GHz, (e) 13.91 GHz, and (f) 14.39 GHz.

conversion) is achieved. While the equal magnitude of the decomposed components $|r_u| = |r_v| \approx 1$ and their phase difference of 90° leads to obtaining the CPC phenomenon. This phase difference usually arises from the orthogonal anisotropy of the MS, which excites different intrinsic modes under u- and v-polarized wave incidence.

To validate the above discussion theoretically, the proposed MS structure is simulated for u- and v-fields components. As structural orthogonal anisotropy does exist along u- and v-axes, thereby remaining independent and providing different co-pol. reflection response of u and v at the same frequency. However, FR4 substrates exhibit higher loss, thereby around 1 dB magnitude of r_u and r_v is visible in the Figures. 5(b) and 5(d). More details of Figure 5(b) reveal that the reflected components' magnitude satisfies $|r_u| = |r_v| \approx 1$, while the phase difference ($\Delta\phi r_{uv} = |\O r_u - \O r_v|$) remains $\approx$180°±35° in bands from 2.41 – 2.48 GHz, 3.16 – 3.46 GHz, 5.80 – 6.59 GHz, 11.64 – 13.75 GHz, resulting in the LTL-RCP conversion. Additionally, $\Delta\phi r_{uv} \approx 90°$ (and its odd multiples) are observed in the frequency bands of 2.33 – 2.38 GHz, 2.55 – 2.99 GHz, 3.69 – 5.37 GHz, 7.13 – 10.92 GHz, 13.95 – 14.25 GHz, 14.93 – 15.17 GHz, and 15.31 – 15.56 GHz, satisfying the condition for the CPC phenomena. A similar trend of equal magnitudes $|r_u| = |r_v|$, and phase differences of $\Delta\phi r_{uv}$ $\approx$180° ± 35° for RCP and $\Delta\phi r_{uv} \approx \pm 90°$ (following an odd multiple) for the CPC phenomenon, are observed for the 15° rotated hourglass design, as shown in Figure 5(d), wherein the CPC frequency bands are obtained at 2.20 – 2.36 GHz, 2.95 – 8.41 GHz, 10.84 – 12.30 GHz, and 14.84 – 15.06 GHz, and RCP conversion from 13.71 to 14.64 GHz. The nature of the CPC can be quantified using Stokes parameters [33], given as:

$$A = |R_{yy}|^2 + |R_{xy}|^2 \quad (5)$$

$$B = |R_{yy}|^2 - |R_{xy}|^2 \quad (6)$$

$$C = 2\,|R_{yy}|\,|R_{xy}|\,cos\Delta\varphi \quad (7)$$

$$D = 2|R_{yy}||R_{xy}|sin\Delta\varphi \quad (8)$$

The normalized ellipticity (e) can be assessed from $e = D/A$ relation, where a +1 value denotes the RHCP and a −1 refers to LHCP conversion. The ellipticity shown in Figures 6(a) and 6(b) verified that the RHCP conversion exists in the frequency bands (2.33 – 2.38 GHz, 3.69 – 5.37 GHz, and 15.31 – 15.56 GHz) for 45°, and (2.20 – 2.36 GHz, 3.75 – 5.65 GHz) for 15° rotated hourglass. While LHCP lies at (2.55 – 2.99 GHz, 7.13 – 10.92 GHz, 13.95 – 14.25 GHz, and 14.93 – 15.17 GHz) for 45°, and (2.95 – 3.12 GHz, 6.64 – 8.41 GHz, 10.84 – 12.30 GHz, and 14.84 – 15.06 GHz) for 15° rotated hourglass, respectively.

It is worth mentioning that the generation of both LTL-RCP conversion and CPC responses is directly associated with the anisotropic nature of the proposed MS, which formed when the hourglass rotated at 45° or 15°. Wherein E_i interaction and collective reflection of the orthogonal components (i.e., E_{ru} and E_{rv}) leads to the generation of different impedances and phase responses. However, due to their symmetric nature w.r.t u- and v-coordinates, the response for either y- or x-polarized (TE- or TM-polarized) E_i will remain the same.

V. CURRENT DISTRIBUTION ANALYSIS

To counter verify the LTL-RCP and CPC characteristics, a current distribution analysis is carried out for 45° and 15° rotated hourglass. The surface current distribution on the top and bottom layers at [2.44 GHz, 3.31 GHz, 6.18 GHz, and 13.50 GHz]$^{45°}$ and [13.91 GHz and 14.39 GHz]$^{15°}$ of the LTL-RCP conversion is shown in Figure 7 At 2.44 GHz and 3.31 GHz [Figures 7(a) and 7(b)], the surface current on the top layer is directed downward along the −v-direction, whereas on the bottom layer, it is opposite to the top layer, along the v- and u-direction. These out-of-phase currents lead to a strong magnetic resonance, causing the surface to function as HIS. In contrast, at 6.18 GHz and 13.50 GHz [Figures 7(c) and 7(d)], the current directions on the top and bottom layers remain in phase, thereby achieving a PEC response. Additionally, at 13.91 GHz and 14.39 GHz [Figures 7(e) and 7(f)], the out-of-phase current is observed on both layers, resulting in HIS behavior. Such a collective

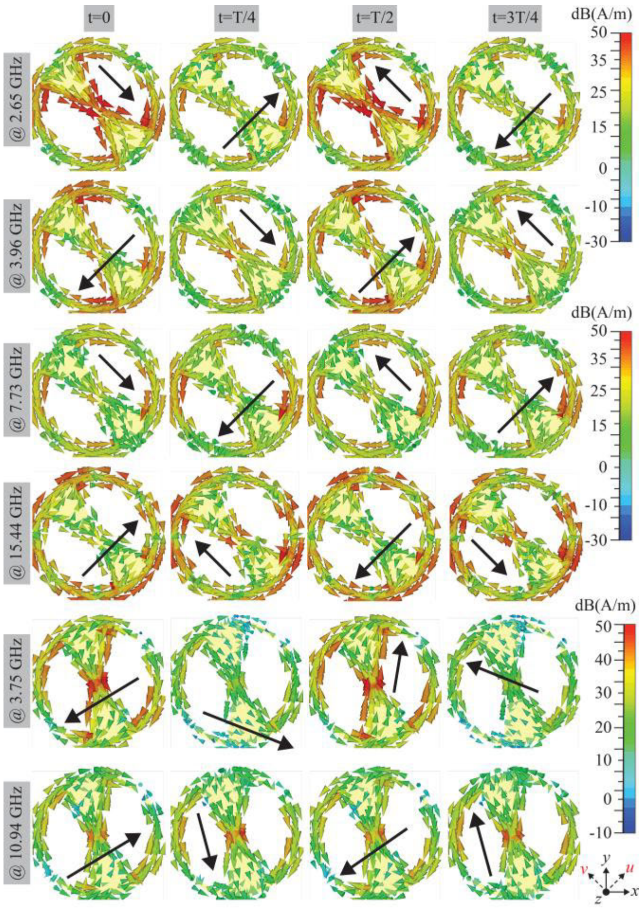

FIGURE 8. Revolving surface current for linear polarization to CP conversion at different frequencies.

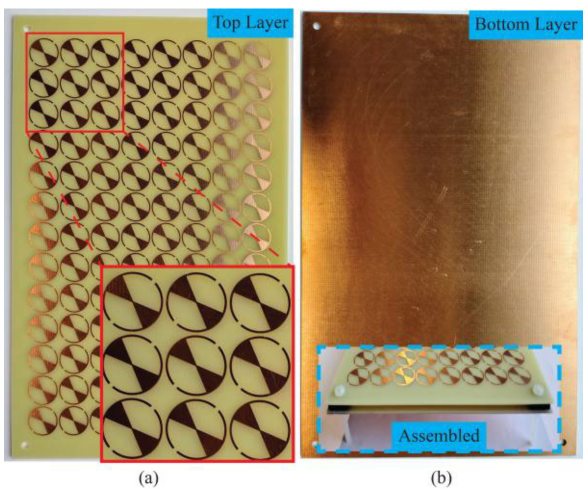

FIGURE 9. Fabricated prototype of the proposed MS: (a) top layer, (b) bottom layer with assembled configuration.

response of HIS and PEC regarding the proposed MS results in obtaining LTL-RCP conversion.

Furthermore, to examine the nature of the CPC mechanism of 45° and 15° rotated hourglass, the surface current, which revolves with a quarter period by 90° is studied and presented in Figure 8. The revolving surface current at [2.65 GHz,

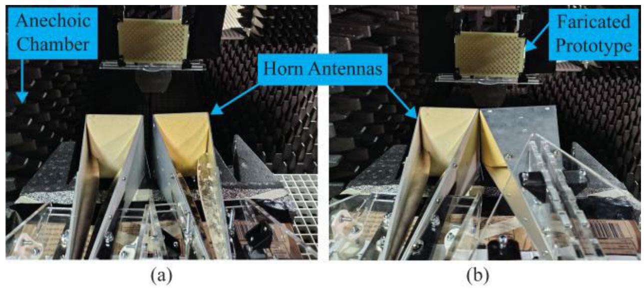

FIGURE 10. Adopted measurement setup for (a) co-pol. and (b) cross-pol. reflection responses.

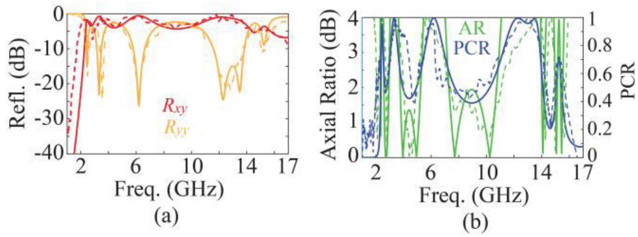

FIGURE 11. Measured (*dotted lines*) and simulated (*solid lines*) responses of (a) co-and cross-pol. reflection (b) PCR and AR.

7.73 GHz]$^{45°}$ and [10.94]$^{15°}$ is in a clockwise direction, verifying the existence of LHCP conversion, whereas counterclockwise currents at [3.96 GHz, 15.44 GHz]$^{45°}$ and [3.75]$^{15°}$ giving birth to the RHCP conversion.

The current distribution analysis indicates that the proposed MS supports two functionalities: CPC and LTL-RCP conversion. The LTL-RCP responses can also be mathematically evaluated through the Jones matrix [34]. For perfect RCP conversion, the following condition must be satisfied: $|R_{xx}| = |R_{yy}| \approx 0$, and $|R_{xy}| = |R_{yx}| \approx 1$. While for CPC, the reflected components must exhibit $|R_{yy}| = |R_{xy}|$, and $\angle R_{yy} - \angle R_{xy} = \pm 90°$. In the following, the relation of co- and cross-pol. reflection can be represented by $\begin{bmatrix} E_{rx} \\ E_{ry} \end{bmatrix} = \begin{bmatrix} R_{xx} & R_{xy} \\ R_{yx} & R_{yy} \end{bmatrix} \begin{bmatrix} E_{ix} \\ E_{iy} \end{bmatrix}$. Based on the simulation results, the reflection matrix for the RCP conversion band can be approximated as: $\begin{bmatrix} 0.049 & 0.938 \\ 0.93 & 0.049 \end{bmatrix}^{45°} \approx \begin{bmatrix} 0 & 1 \\ 1 & 0 \end{bmatrix}^{45°}$ and $\begin{bmatrix} 0.036 & 0.91 \\ 0.91 & 0.036 \end{bmatrix}^{15°} \approx \begin{bmatrix} 0 & 1 \\ 1 & 0 \end{bmatrix}^{15°}$.

VI. EXPERIMENTAL VALIDATION

To validate the performance of the proposed MS, a prototype with 8 × 13-unit cells was fabricated using standard PCB technology and assembled with air spacers between the dielectric substrate and metallic backplate, as shown in Figures 9(a) and 9(b). The overall physical dimensions of the prototype are 127 × 203.2 × 6.7 mm^3. All measurements were carried out in an anechoic chamber, where a pair of horn antennas (linearly polarized) connected to a vector network analyzer (MS4644B) and a sample holder is used, as shown in Figures 10(a) and 10(b). A far-field distance

TABLE 1. Proposed multiband MS versus state-of-the-art benchmark designs.

Ref.	Profile (at λ_h^3)	PC type: RCP (GHz)	PC type: CPC (GHz)	No. of bands*: RCP	No. of bands*: CPC	Total number of RCP and CPC bands	Orientation **	Use of diode***	ML
[10]	0.49×0.49×0.22	NR	5.85–6.85, 7.11–9.44	0	2	2	No	Yes	3
[12]	0.48×0.48×0.18	7.30–8.90, 19.40–4.92, 8.9–13.22.	9.79–17.42, 7.60–8.30, 14.71–16.83	3	3	6	No	Yes	2
[13]	0.73×0.73×0.27	5.96–15.34	6.05–14.76	1	1	2	No	Yes	2
[14]	0.38×0.38×0.63	2.48–3.79	2.41–3.76, 2.48–3.79	1	2	3	No	Yes	4
[15]	0.46×0.46×0.13	5.6–6.5, 9.6–11.9	5.4, and 6.9–8.9	2	2	4	No	No	1
[16]	0.92×0.92×0.18	9–10.6, 15.9–16, 18.6–22.9, 23.7–23.8, 25.9–26.9	8.6–8.8, 10.9–11.4, 15.6–15.8, 16.8–17.7, 22.9–23, 23.3–23.4, 25.6–25.7, 27.3–27.5	5	8	13	No	No	1
[17]	0.43×0.43×0.14	5.9–6.4, 8.7–17.7	6.7–8.4	2	1	3	No	No	1
[18]	0.65×0.65×0.12	5.47–5.68, 7.86–8.84, 14.68–16.83	5.30–5.41, 5.77–7.58, 9.27–13.91, 17.53–19.59	3	4	7	No	No	1
[19]	0.55×0.55×0.16	5.3–5.4, 7.2–8, 12.3–13.76	5.1– 5.2, 5.6–6.85, 8.8–11.2, 14.9–20.2	3	4	7	No	No	1
[20]	0.11×0.11×0.15	16.2–17.2, 23.0–25.4, 40.3–54.35	16.1–16.55, 17.5–22.15, 26.65–37.75, 55.6–59.8	3	4	7	No	No	1
[21]	0.49×0.49×0.05	8.14–8.25, 10.23–10.60, 13.90–14.08 16.59–16.71	7.8–8.10, 8.32–10.04, 10.80–13.75, 14.19–14.53, 16.22–16.52, 16.77–17.18	4	6	10	No	No	1
[22]	0.43×0.43×0.13	9.46–11.63, 15.86–17.28.	12.50–15.26	2	1	3	No	No	1
[23]	0.42×0.42×0.10	12.16 – 12.81, 15.28 – 15.66, 17.94 – 18.73	10.90–11.90, 15.84–17.63, 13.12–15.08, 19.11–21	3	4	7	No	No	1
[24]	0.83×0.83×0.20	6.3–6.5, 9.1–15.4, 25.3–29, 31–31.8, 35.7–35.9	6.60–6.67, 8.70–8.95, 15.69–16.25, 21.35–21.55, 24.15–24.97, 29.52–30.63, 32.00–32.07, 35.47–35.56	5	8	13	No	No	1
[25]	0.48×0.48×0.07	5.18–5.23	10.64–10.82, 12.25–12.47, 14.42–14.67	1	3	4	No	No	1
[26]	0.25×0.25×0.08	13.5–18.0, 18.0–26.5, 26.5–38.5	14.57–15.65, 27.47–33.85, 17.27–23.92, 35.87–38.32	3	4	7	No	No	1
TW	0.72×0.72×0.26	**45°: 2.41–2.48, 3.16–3.46, 5.80–6.59, 11.64–13.75,**	**2.33–2.38, 2.55–2.99, 3.69–5.37, 7.13–10.92, 13.95–14.25, 14.93–15.17, 15.31–15.56,**	**5**	**11**	**16**	**Yes**	No	**1**
		15°: 13.71–14.64	**2.20–2.36, 2.95–8.41, 10.84–12.30, 14.84–15.06**						

* $\boldsymbol{\lambda_h}$**:** Highest operating frequency, **ML:** metasurface layers, **TW:** this work.
* **No. of bands** = number of RCP conversion and CPC bands.
** **Orientation** = Orientation controlled functionalities in a single MS deign.
*** **Use of diode** = use of diode to obtain RCP conversion and CPC functionalities.

$d = 2D^2/\lambda$ is kept between the horn antennas and the prototype to ensure uniform plane wave illumination. Therein, D is the prototype dimension, and λ corresponds to the highest operating frequency. For the co-pol. and cross-pol. reflection measurements, we first recorded the free space reflection measurements from the PEC plate for calibration, and then subtraction was performed from the measured results of the MS prototype. While measuring the co-pol. reflection (cross-pol. reflection) coefficients, the horn antennas were positioned parallel (orthogonal) in front of the proposed MS array to record the resultant reflected waves.

The finalized measured co- and cross-pol. reflection results of the proposed MS array are plotted in Figure 11(a). Wherein, the co-pol. reflection $R_{yy} \leq -10$ dB at 2.41 – 2.48 GHz, 3.16 – 3.46 GHz, 5.80 – 6.59 GHz, 11.64 – 13.75 GHz frequency bands, while the corresponding cross-pol. reflection magnitude is around −1 dB, confirming that the proposed MS achieved the LTL-RCP conversion. Furthermore, the same reflection magnitudes of around 3 dB is observed at 2.33 – 2.38 GHz, 2.55 – 2.99 GHz, 3.69 – 5.37 GHz, 7.13 – 10.92 GHz, 13.95 – 14.25 GHz, 14.93 – 15.17 GHz, and 15.31 – 15.56 GHz, validating the CPC condition. In addition, the measured phase and magnitude values of the reflected co- and cross-pol. components were further used to compute the AR and PCR, as plotted in Figure 11(b). Overall, a good degree of consistency between measurements and the simulated results is observed; minor deviations can be attributed to imperfections in fabrication, misalignment of antennas during measurements, finite array size of the fabricated MS array, and dielectric constant tolerances.

Since the 15° design is merely a rotated hourglass version of the same validated unit cell, and no geometrical or material modification is introduced. Therefore, the measured 45° prototype is sufficient to experimentally confirm the operating principle, while the 15° case is rigorously verified through parametric full-wave EM simulations.

To emphasize the novelty of the proposed MS unit cell, its performance is compared with that reported in the literature, as summarized in Table 1. The advantages of the proposed MS over existing works can be highlighted as follows:

1. It offers more compact footprints than the designs reported in [13], [14], and [16].
2. It features lower structural complexity than the designs in [10], [12], [13], and [14], in terms of not incorporating any active elements while retaining multiband performance. In addition, compared with [10], [12], [13], and [14], the proposed MS work includes fewer substrate layers.
3. While existing designs in [10], [12], [13], [14], [15], [16], [17], [18], [19], [20], [21], [22], [23], [24], [25], and [26] achieve multiband RCP conversion and CPC performance by incorporating PIN diodes or employing a single-layer multi-resonance structure. However, the proposed work introduces an additional feature of orientation-controlled functionalities without altering the physical geometry of the surface. This feature is absent in previous studies.

VII. CONCLUSION

This study proposes and experimentally validates an anisotropic MS, providing multifunctionality including RCP conversion and CPC responses across multiple frequency ranges spanning the S-, C-, X-, and Ku-bands. The proposed work employs a truncated circular ring with an hourglass structure on a single substrate layer. Both proposed functionalities (LTL-RCP conversion and CPC) with different bandwidths and at different frequency bands from 2.2 to 15.56 GHz are achieved when only the hourglass structure of the unit cell rotates at 15° and 45° orientation, enhancing the MS selectivity and flexibility. To verify both functionalities, a current distribution analysis is performed and presented to examine its working principle. Owing to its flexible multiband and multifunctional capabilities, the proposed MS work might be considered a strong candidate for advanced communication systems spanning across the S-, C-, X-, and Ku-bands. Additionally, its orientation-controlled feature enables flexible polarization manipulation without the need for active components, making it attractive for compact wireless communication and radar applications.

Although the design promises optimal performance primarily under normal incidence conditions. However, its performance tends to degrade at oblique angles due to the spatial dispersion effect generated between the air space and the dielectric substrates [5], [28]. Usually, smaller unit sizes contribute to overcoming the spatial dispersion effect and provide better angular stability; therefore, our future research will emphasize design miniaturization to retain wide angular stability beyond 60° or higher.

REFERENCES

[1] Z. Wang, S. Liu, and Y. Dong, "Low-profile multifunctional pattern reconfigurable antenna using periodic capacitor-loaded surface for 5G and beyond," *IEEE Trans. Antennas Propag.*, vol. 70, no. 5, pp. 3277–3286, May 2022.

[2] J.-W. Xu, F.-C. Chen, and K.-R. Xiang, "Synthesis design of bandpass frequency selective surface with flat in-band group delay response," *IEEE Antennas Wireless Propag. Lett.*, vol. 25, pp. 324–328, 2026.

[3] Y. Shang, X. Lei, C. Liao, and J. Chen, "Frequency-selective structures with suppressed reflection through passive phase cancellation," *IEEE Trans. Antennas Propag.*, vol. 68, no. 2, pp. 1192–1197, Feb. 2020.

[4] X. Yang, E. Wen, D. Bharadia, and D. F. Sievenpiper, "Multifunctional metasurface: Simultaneous beam steering, polarization conversion, and phase offset," *IEEE Trans. Antennas Propag.*, vol. 72, no. 5, pp. 4589–4593, May 2024.

[5] M. Nasir, S. Koziel, and A. Iftikhar, "A highly miniaturized and wide angularly stable antenna-filter-antenna-based polarization rotating frequency selective surface for radar systems," *IEEE Access*, vol. 13, pp. 154729–154738, 2025.

[6] M. Fawaz, B. Sanz-Izquierdo, and E. A. Parker, "Staple-based frequency-selective surfaces for electromagnetic control in buildings," *IEEE Trans. Antennas Propag.*, vol. 73, no. 12, pp. 10057–10066, Dec. 2025.

[7] M. K. T. Al-Nuaimi, G.-L. Huang, W. G. Whittow, R.-S. Chen, and S.-W. Wong, "Realization of single-layer Fourier phased metasurfaces for wideband RCS reduction," *IEEE Antennas Wireless Propag. Lett.*, vol. 22, pp. 1179–1183, 2023.

[8] W. Li, Y. M. Wang, Y. Hei, B. Li, and X. Shi, "A compact low-profile reconfigurable metasurface antenna with polarization and pattern diversities," *IEEE Antennas Wireless Propag. Lett.*, vol. 20, pp. 1170–1174, 2021.

[9] H. Li, C. Wang, and N. Lu, "A wideband metasurface antenna using multi-mode radiator for broadband wireless communication applications," *IEEE Access*, vol. 12, pp. 74081–74086, 2024.

[10] H. Yang, Y. He, M. S. Tong, L. T. Guo, P. Li, and Y. J. Zhang, "A reflection-transmission multifunctional polarization conversion metasurface," *IEEE Trans. Antennas Propag.*, vol. 72, no. 6, pp. 5099–5109, Jun. 2024.

[11] J. Lin, D. Li, Y. Gao, and W. Yu, "Transmission–reflection-integrated multifunctional metasurface for polarization reconfigurability," *IEEE Trans. Antennas Propag.*, vol. 73, no. 11, pp. 9030–9039, Nov. 2025.

[12] Q. Guo, F. Hao, M. Qu, J. Su, and Z. Li, "Multiband multifunctional polarization converter based on reconfigurable metasurface," *IEEE Antennas Wireless Propag. Lett.*, vol. 23, pp. 1241–1245, 2024.

[13] H. Yang, S. C. Wang, P. Li, Y. He, and Y. J. Zhang, "A broadband multifunctional reconfigurable polarization conversion metasurface," *IEEE Trans. Antennas Propag.*, vol. 71, no. 7, pp. 5759–5767, Jul. 2023.

[14] H. Zhou, X. Yu, P. Wang, Y. Wang, and Z. Yan, "Wideband linear-to-multi-polarization converter based on active metasurface," *IEEE Trans. Antennas Propag.*, vol. 71, no. 6, pp. 5246–5255, Jun. 2023.

[15] M. A. Shah, M. S. Ali, A. Naeem, S. Ullah, M. Imran, Q. Abbasi, and H. Arslan, "Multifunctional metasurface for linear-to-linear and linear-to-circular polarization conversion," *IEEE Access*, vol. 14, pp. 18169–18180, 2026.

[16] H. Rauf, B. Kamal, S. Ullah, U. Ali, and L. Matekovits, "Experimental validation of a multi-functional metasurface for 5G and satellite communication," *IEEE Access*, vol. 13, pp. 55476–55486, 2025.

[17] A. Ahmed, Q. Cao, M. I. Khan, F. Ahmed, and F. A. Tahir, "A multifunctional broadband polarization rotator based on reflective anisotropic metasurface," *Phys. Lett. A*, vol. 470, May 2023, Art. no. 128785.

[18] S. Ghosh, J. Ghosh, M. Santoshkumar Singh, and A. Sarkhel, "A low-profile multifunctional metasurface reflector for multiband polarization transformation," *IEEE Trans. Circuits Syst. II: Exp. Briefs*, vol. 70, no. 1, pp. 76–80, Jan. 2023.

[19] F. Ahmed, M. I. Khan, and F. A. Tahir, "A multifunctional polarization transforming metasurface for C-, X-, and K-band applications," *IEEE Antennas Wireless Propag. Lett.*, vol. 20, pp. 2186–2190, 2021.

[20] J. Zafar, H. Z. Khan, A. Jabbar, J. U. R. Kazim, M. U. Rehman, A. M. Siddiqui, Q. H. Abbasi, and M. A. Imran, "Asymmetric multi-band reflective metasurface for linear and circular polarizations conversion in Ku, K, Ka, and U bands," *Sci. Rep.*, vol. 15, no. 1, p. 4977, Feb. 2025.

[21] N. Pouyanfar, J. Nourinia, C. Ghobadi, and V. Nayyeri, "Low-profile reflective surface for multi-band linear-to-linear and linear-to-circular polarization conversion," *IEEE Access*, vol. 11, pp. 135159–135165, 2023.

[22] S. Hafeez, J. Yu, A. Majeed, F. A. Umrani, and Y. Huang, "Optically transparent coding metasurface with dual-polarization conversion and RCS reduction characteristics," *IEEE Access*, vol. 13, pp. 30779–30788, 2025.

[23] H. Z. Khan, A. Jabbar, J. Ur Rehman Kazim, J. Zafar, M. Ur-Rehman, M. A. Imran, and Q. H. Abbasi, "Reflective metasurface for multi-band polarization conversion for satellite applications in 6G networks," *IEEE Open J. Antennas Propag.*, vol. 6, pp. 332–343, 2025.

[24] M. I. Khan, Y. Chen, B. Hu, N. Ullah, S. H. R. Bukhari, and S. Iqbal, "Multiband linear and circular polarization rotating metasurface based on multiple plasmonic resonances for C, x and k band applications," *Sci. Rep.*, vol. 10, no. 1, p. 17981, Oct. 2020.

[25] S. M. Q. A. Shah, N. Shoaib, F. Ahmed, A. Alomainy, A. Quddious, S. Nikolaou, M. A. Imran, and Q. H. Abbasi, "A multiband circular polarization selective metasurface for microwave applications," *Sci. Rep.*, vol. 11, no. 1, p. 1774, Jan. 2021.

[26] H. Z. Khan, A. Jabbar, J. U. R. Kazim, M. U. Rehman, M. A. Imran, and Q. H. Abbasi, "Multi-band ultrathin reflective metasurface for linear and circular polarization conversion in Ku, K, and Ka bands," *Commun. Eng.*, vol. 3, no. 1, p. 124, Sep. 2024.

[27] S. Ghosh, P. M. Sainadh, A. Sarkhel, and S. Ghosh, "Wideband superstrate-loaded metasurface-based multifunctional polarization converters," *IEEE Antennas Wireless Propag. Lett.*, vol. 24, pp. 1337–1341, 2025.

[28] M. Nasir, S. Koziel, and A. Pietrenko-Dabrowska, "A multifunctional bi-anisotropic metasurface with reflection-transmission polarization conversion and narrow bandpass transmission characteristics," *Sci. Rep.*, vol. 16, p. 13838, Mar. 2026.

[29] L. Wang, S. Liu, X. Kong, H. Zhang, Q. Yu, Y. Wen, and D. Wang, "A multifunctional frequency-selective polarization converter for broadband backward-scattering reduction," *IEEE Trans. Antennas Propag.*, vol. 69, no. 5, pp. 2833–2841, May 2021.

[30] A. Khan, B. Kamal, S. Ullah, A. Ahmad, and D. Y. Choi, "Dual-band cross-polarization and linear-to-circular polarization converting metasurface," *Res. Phys.*, vol. 73, Jun. 2025, Art. no. 108222.

[31] M. Nasir, A. Iftikhar, S. M. Abbas, R. Saleem, M. F. Shafique, and M. Alathbah, "A wideband broadside coupled Yagi antenna and arrays system for Ku band applications," *IEEE Access*, vol. 11, pp. 126967–126978, 2023.

[32] M. Nasir, A. Iftikhar, M. F. Shafique, B. Saka, S. Nikolaou, and D. E. Anagnostou, "Broadband dual-podal multilayer Vivaldi antenna array for remote sensing applications," *IET Microw., Antennas Propag.*, vol. 17, no. 7, pp. 505–517, May 2023.

[33] M. I. Khan, Z. Khalid, and F. A. Tahir, "Linear and circular-polarization conversion in X-band using anisotropic metasurface," *Sci. Rep.*, vol. 9, no. 1, p. 4552, Mar. 2019.

[34] C.-Y. Hsu, L.-T. Hwang, T.-S. Horng, S.-M. Wang, F.-S. Chang, and C. N. Dorny, "Transmitarray design with enhanced aperture efficiency using small frequency selective surface cells and discrete Jones matrix analysis," *IEEE Trans. Antennas Propag.*, vol. 66, no. 8, pp. 3983–3994, Aug. 2018.

MUHAMMAD NASIR received the B.S. and M.S. degrees in electrical engineering from COMSATS University Islamabad (CUI), Pakistan, in 2015 and 2020, respectively. He is currently pursuing the Ph.D. degree with the Department of Engineering, Reykjavík University, Iceland. His research interests include multilayer antennas array and metasurfaces.

SLAWOMIR KOZIEL (Fellow, IEEE) received the M.Sc. and Ph.D. degrees in electronic engineering from Gdańsk University of Technology, Poland, in 1995 and 2000, respectively, the M.Sc. degree in theoretical physics, in 2000, the M.Sc. degree in mathematics, in 2002, and the Ph.D. degree in mathematics from the University of Gdańsk, Poland, in 2003. He is currently a Professor with the Department of Engineering, Reykjavík University, Iceland. His research interests include CAD and modeling of microwave and antenna structures, simulation-driven design, surrogate-based optimization, space mapping, circuit theory, analog signal processing, evolutionary computation, and numerical analysis.

ANNA PIETRENKO-DABROWSKA (Senior Member, IEEE) received the M.Sc. and Ph.D. degrees in electronic engineering from Gdańsk University of Technology, Poland, in 1998 and 2007, respectively. She is currently an Associate Professor with Gdańsk University of Technology. Her research interests include simulation-driven design, design optimization, control theory, modeling of microwave and antenna structures, and numerical analysis.